Automated ultrasonic-based diagnosis of concrete compressive damage amidst temperature variations utilizing deep learning

Lei Wang [a], Shanchang Yi [a,b], Yang Yu [c,*], Chang Gao [a], Bijan Samali [b]

[a] *School of Civil Engineering, Changsha University of Science & Technology, Changsha 410114, China*

[b] *Centre for Infrastructure Engineering, School of Engineering, Design and Built Environment, Western Sydney University, Sydney, NSW 2747, Australia*

[c] *Centre for Infrastructure Engineering and Safety, School of Civil and Environmental Engineering, The University of New South Wales, Sydney, NSW 2052, Australia*

ARTICLE INFO

ABSTRACT

Ultrasonic-based non-destructive testing technologies have been extensively applied for detection of internal damage in concrete. However, it is vulnerable to environmental temperature variations. An automated ultrasonic-based diagnosis approach integrating the continuous wavelet transform, and the transfer learning enhanced deep convolutional neural networks is proposed to evaluate compressive damage amidst temperature variations. The ultrasonic tests were conducted on pre-damaged concrete specimens, considering both temperature variations and damage levels as variables. The results indicate that the temperature fluctuations significantly influence the ultrasonic parameters of concrete compression damage. The proposed method effectively identifies the concrete damage state amidst temperature variations. Furthermore, it is recommended that the temperature range within the training set should uniformly cover the expected temperature range throughout the lifespan of concrete structures. This study offers novel perspectives for ultrasonic testing of concrete subjected to environmental variations.

1. Introduction

Concrete structures have been widely used in construction, bridges and many other engineering fields, whose safety-performance and workability exhibit significant effect on the society and personal safety. The health status monitoring and assessment of the concrete structures have exhibited significance during the maintenance process of concrete structures. With its robust penetration ability and high sensitivity to defects like cracking, ultrasonic testing offers promising prospects for detecting internal damage in concrete structures [1].

In the last few decades, a variety of ultrasonic characterization methods have been developed for detection of internal damage in concrete structures [2–4]. According to the principles of signal analysis, these methods can be mainly divided into linear ultrasonic techniques and nonlinear ultrasonic techniques [5–7]. Linear ultrasonic techniques characterize damage based on the time-domain parameters such as the amplitude, energy, and wave velocity [8,9], which are typically considered to have lower sensitivity. Nonlinear ultrasonic techniques, utilizing frequency domain features, offer high sensitivity to subtle changes in the structural state. The more commonly used nonlinear ultrasonic techniques include the higher harmonic method [10–12], nonlinear resonant ultrasonic

---

method [13–15]. In addition, due to its high sensitivity to subtle changes, the coda wave method has become a research hotspot in the field of non-destructive testing for concrete structures [16–18]. Extensive studies indicate that ultrasonic testing has become an important means of detecting internal damage in concrete structures.

The traditional methods characterize the trend of damage development by extracting one or several parameters, resulting in erroneous detection results amidst environmental temperature variations. Typically, temperature increase would cause thermal expansion and Young's modulus changes of the substrate, affecting ultrasonic parameters such as wave velocity and amplitude. Scalea et al. [19] observed that temperature increase would significantly affect the amplitude, which increases with temperature increase within −40 ℃ to 20 ℃ and decreases with temperature increase within 20 ℃ to 60 ℃. Putkis et al. [20] found that the amplitude increase up to 30 % within −10 ℃ to 30 ℃ and temperature variations cause changes in guided wave velocity. Niederleithinger et al. [21] used the coda wave interferometry (CWI) to measure the influence of the temperature changes ranging from 0 ℃ to 50 ℃ on the ultrasonic wave velocity of concrete samples. The study concluded that the velocity variation exceeds 3 % with temperature changes of 50 ℃. Zhao et al. [22] revealed that the relative nonlinear parameters increase with the temperature rise from 15 ℃ to 40 ℃ in concrete.

Concrete structures are universally exposed to the natural environment where temperature fluctuations can be significant. In order to enhance immunity of the ultrasonic testing to the impact of temperature fluctuations, several methods have been developed, e.g., the baseline signal stretch (BSS) method [23,24], the optimal baseline selection (OBS) method [24,25] and the thermally-compensated method based on reference specimen [26,27]. The BSS compensates for the effects of temperature Fourier changes on wave speed and thermal expansion by stretching the measurement signal to match the baseline signal. This method would be effective when the temperature difference between the measurement signal and the baseline signal is small. When the temperature difference is large, the stretching signal would change the shape of the wave packet, resulting in the failure of BSS [28]. The OBS was developed to address this issue, it involves acquiring multiple baseline signals across the expected temperature range throughout the lifespan of the concrete structures. The reasonable temperature step in a baseline dataset was suggested to be 1 to 2 ℃ [25]. However, in the context of civil engineering, significant temperature fluctuations exist in the concrete structures. Therefore, the OBS may not be feasible because obtaining sufficient baseline signals that precisely match the exact temperature of interest is challenging. The thermally-compensated method relies on a referenced specimen to obtain wave speed variations related to temperature variations. However, the effectiveness of the thermally-compensated method is dubious due to the scarcity of referenced specimens unaffected by other disturbances [21].

Thanks to the development of deep learning (DL) technologies, data-driven-based surrogate models for concrete damage detection have been extensively studied [29–31]. The deep learning technologies have been applied for ultrasonic evaluation of thermal damages of the concrete subjected to high temperatures [32], the ultrasonic monitoring of concrete-rock interface debonding [33] and the ultrasonic detection of internal defects in reinforced concrete [34]. However, existing ultrasonic diagnostics combined with DL were conducted in environments without considering temperature variations. The impact of temperature changes on the performance of DL models is not well-established. DL methods are adept at autonomously extracting optimal features from different data with the same label, providing a potential alternative solution to the aforementioned issues [35]. However, with the increase in the depth of architecture of DL models, the number of free parameters also increases drastically. For ultrasonic diagnosis tasks, training a large DL network from scratch is challenging, since it typically requires a large amount of labeled data and computational resources. Transfer learning (TL) technique can effectively address this issue. Instead of training a neural network model completely with random initialization, TL uses fine-tuning techniques to adjust a pre-trained network to adapt to new tasks. This approach allows the model to learn high-level features from the pre-trained network, significantly reducing the amount of data and computational resources required. TL technique has been successfully applied in multiple fields, e.g., bearing fault identification [36,37], machine vision [38,39], bridge damage detection based on dynamic behavior [40,41]. As of now, there have been limited reports on the application of TL technique in the field of ultrasonic diagnosis.

This study introduces a hybrid approach to achieve automated ultrasonic-based diagnosis of concrete compressive damage amidst temperature variations. The hybrid approach integrates ultrasonic sweep frequency testing, continuous wavelet transform, and transfer learning enhanced deep convolutional neural networks. The effectiveness of the proposed method is verified through ultrasonic testing experiments performed on concrete specimens with pre-existing compressive damage, amidst varying temperature conditions. Furthermore, the study investigates how the distribution of temperatures in the training set affects the performance of the model. Overall, the novel contributions of this paper may be concluded as: 1) Experimental investigations demonstrate the significant interference caused by temperature fluctuations on the ultrasonic characterization of compressive damage in concrete; 2) This study provides the first evidence of the capability of ultrasonic testing combined with DL in overcoming the effects of environmental temperature fluctuations; 3) The impact of temperature distribution within the training set on the performance of DL models has been analyzed. The analysis provides valuable recommendations for the preparation of datasets for practical applications.

2. Theoretical background

2.1. Continuous wavelet transform

Continuous wavelet transform (CWT) is an excellent method for signal time–frequency decomposition. The use of adaptively sized time–frequency windows overcomes the limitation of fixed window sizes in the Short-Time Fourier Transform (STFT). This allows it to provide more precise frequency information, especially in capturing local features within the signal. CWT decomposition of a one-dimensional signal $x(t)$ can be expressed as [42]:

$$CWT(a, \tau) = \frac{1}{\sqrt{a}} \int_{-\infty}^{\infty} x(t)\psi\left(\frac{t-\tau}{a}\right)dt = \langle x(t), \psi_{a,\tau}(t)\rangle \tag{1}$$

where a is the scale index used to control the scaling of wavelet function, τ is the translation parameter used to control time-shifting and $\psi_{a,\tau}(t)$ is the wavelet basis function. There are many different forms of wavelet basis functions, which include but are not limited to Morlet, Haar, Daubechies, Symlet, and Coiflet. In this research, the Coiflet is employed, benefiting from its excellent time–frequency localization characteristics and good resolution in frequency and time.

2.2. Deep convolutional neural networks

Deep convolutional neural networks (DCNNs) find extensive application in handling tasks related to images [39]. The DCNNs architecture consists of multiple sets of convolutional layers, pooling layers, and fully connected layers. Each layer uses a set of convolution kernels to perform multiple transformations, and then uses the pooling layer to reduce the data dimension, which reduces the computational complexity of the network while maintaining translation invariance. Even if there is a small time–frequency movement in the image, the change feature can be extracted. DCNNs commonly employ gradient descent to minimize the loss function. Subsequently, the network weights and biases layers are adjusted by layer during iterative training, enhancing the generalization capability of the network.

In convolutional layers, a series of filters (also known as kernels) are used to extract features from the input data, such as edges, colors, textures, etc. The filters slide over the input data, computing dot products between the filter weights and the input values. The result is a feature map that highlights important patterns and local dependencies in the data. The features learned by each convolutional layer become progressively more abstract as the network depth increases, enabling DCNNs to recognize and understand complex patterns and objects in images. The general formula for a convolutional layer is as follows [43]:

$$C_i = \sigma\left(\sum_{j=1}^{F} \omega_j * C_{i-1,j} + b_i\right) \tag{2}$$

where C_i represents the ith feature map; F represents the number of filters in the convolutional layer; ω_j represents the jth filter; $C_{i-1,j}$ represents the jth feature map from the previous layer; "*"denotes the convolution operation; b_i represents the ith bias term; σ represents the activation function.

The role of the pooling layer is to reduce the amount of computation and the number of parameters while preserving the most important information in the feature map. This helps to enhance generalization ability of the network and reduce the risk of overfitting. The general formula for a max pooling layer is as follows [43]:

$$P_{i,j} = \max_{(m,n)\in R_{i,j}} C_{i,m,n} \tag{3}$$

where $P_{i,j}$ represents the output of the ith max pooling layer and jth feature map; $R_{i,j}$ represents the receptive field of the ith max pooling layer and jth feature map; $C_{i,m,n}$ represents the input to the ith max pooling layer and jth feature map at position (m,n).

Fully connected layers are typically positioned at the end of the network, capable of integrating local features extracted by previous convolutional and pooling layers. They learn the complex relationships between these features and map the learned high-level features to the final output categories. The general formula for FC layer is as follows [43]:

$$y = \sigma(\mathbf{W}x + b) \tag{4}$$

where y represents the output of the FC layer; $\mathbf{W}$ represents the weight matrix; x represents the input vector of FC layer; b represents the bias vector.

2.3. Transfer learning and fine-tuning strategy

It is well known that DCNNs rely on large amounts of training data to effectively extract features from raw data. However, in practical engineering scenarios, acquiring a sufficient number of ultrasonic to train a deep architecture from the ground up is quite challenging. DCNNs comprise a substantial number of weights that are initialized randomly before training process. These weights are then updated iteratively using labeled data and the loss function. The iterative update of all weights is highly time-consuming. In the presence of limited training data, DCNNs run the risk of overfitting to the training data. The training model for a particular problem is modified and adapted by TL method to effectively tackle new, related problems.

Fine-tuning is a commonly used transfer learning method. For DCNNs, the initial convolutional layers typically focus on extracting low-level features like texture, corners, and colors, while the last few convolutional layers are responsible for capturing higher-level, abstract, and task-specific features. Consequently, during the training of the model, the parameters of the last few convolutional layers are fine-tuned, while the parameters of the initial convolutional layers remain unaltered. Fine-tuning a pre-trained network mainly includes three steps: a) Train DCNNs on a large dataset such as ImageNet to form a pre-trained DCNN model; b) Transfer the parameters of the pre-trained model to the new model; c) Leverage a small quantity of task data for training new models in order to enhance the capability to extract features more effectively.

In this research, twelve commonly used pre-trained DCNNs, which were trained on ImageNet. The ImageNet is a large-scale visualization database designed for visual object recognition software research [39]. These models are employed as the backbones to develop diagnosis models for concrete compressive damage amidst temperature variations based on TL, including AlexNet, DenseNet, EfficientNet-b0, GoogLeNet, Inception-v3, MobileNet-v2, ResNet-18, ResNet-50, ShuffleNet, SqueezeNet, VGG-16, VGG-19. The parameter information is presented in Table 1, and the details of the network architecture can be found in [39].

3. Ultrasonic testing for concrete compressive damage amidst temperature variations

3.1. Materials and specimens

To investigate the impact of temperature changes on the ultrasonic testing for concrete compressive damage, six concrete cubic specimens ($150 \times 150 \times 150$ mm^3) were cast, the concrete mix proportions are given in Table 2. All specimens underwent a curing period of 28 days in an indoor environment, maintained at a temperature of 25 ℃ and a humidity of 100 %. Subsequently, to determine the appropriate loading force for each step, three specimens were used for compressive strength testing, and the average compressive strength is 37.6 MPa. The remaining three specimens, after being fitted with sensors, were placed in a drying oven at 50 ℃. This process aimed to eliminate the effects of ongoing hydration reactions within the concrete and potential impacts of temperature changes on the sensor adhesive layer.

3.2. Setup and procedure

The overall experimental setup is depicted in Fig. 1. The entire experiment consists of three parts: introducing predetermined damage, changing temperature, and ultrasonic testing. For introducing predetermined damage, a universal testing machine was used to induce incremental damage in multiples of 4.44 MPa. Upon reaching the target load at each stage, the specimens were completely unloaded. In the part of changing temperature, the specimens were placed in a programmable temperature and humidity chamber, set initially at 20 ℃ with a humidity of 70 %. In this environment, the specimens were allowed to rest undisturbed for 2 h to acclimate to the environmental changes and to fully mitigate slow dynamic effects. [16] Subsequently, the environmental temperature was progressively increased from 20 ℃ to 40 ℃, in 2 ℃ increments. To ensure a uniform temperature distribution across each specimen, the ultrasonic testing was conducted 20 min after implementing each temperature increment. [44] It is worth noting that the changing temperature experiments were conducted on the specimens in both the undamaged state and damage increment states. The entire experimental procedure is illustrated in Fig. 2.

A pair of smart aggregate sensors was employed [45], where, one serving to excite and the another to receive. These sensors were attached to the centers of two adjacent faces of the cubic specimen using epoxy resin. The excitation signal, a swept frequency signal ranging from 80 kHz to 160 kHz, had a duration of 0.4 ms and an amplitude of 10 V. It was generated by a function generator (Model AFG31022- Tektronix). On the receiving end, a pre-filter amplifier (OPLABBOX 2.0) was used for high-pass filtering at 40 kHz and amplification at 60 db. Ultrasonic waves were collected and stored using an industrial computer (NI PXI-8119) equipped with an NI data acquisition card (NI PXI-5105), which had a sampling rate of 10 MHz and a sampling length of 55,002. The function generator facilitated synchronized triggering.

In this experiment, after measuring the signals at all temperatures in the undamaged state, predetermined damages were introduced in increments of 4.44 MPa, as shown in Fig. 2. Specimen 1 and Specimen 2 were nearly fractured after subjecting to 8 damage increments, making it impossible to conduct variable temperature tests. Specimen 3 was crushed before reaching the eighth damage increment. Consequently, for each specimen, ultrasonic signals were collected for 8 damage states, including the undamaged state and 7 damage increment states, under 11 different temperature conditions.

4. Evaluation of the impact of compressive damages and temperature variations on ultrasonic parameters

4.1. Peak-to-peak value and signal energy

The ultrasonic waveforms obtained from the experiment are illustrated in Fig. 3. Due to space constraints, Fig. 3 partially presents the ultrasonic waveforms obtained from specimen 1 under different temperature conditions and various damage states, as detailed in the figure labels. It can be observed that, compared to the undamaged state, the ultrasonic waveforms exhibit decay after being

Table 1
Parameter information of pre-trained DCNNs for ultrasonic diagnosis.

Model	Depth	Dimension of inputs	Number of Parameters (million)	Model	Depth	Dimension of inputs	Number of Parameters (million)
AlexNet	8	227×227	61	ResNet-18	18	224×224	11.7
DarkNet-19	19	256×256	20.8	ResNet-50	50	224×224	25.6
EfficientNet-b0	82	224×224	5.3	ShuffleNet	50	224×224	1.4
GoogLeNet	22	224×224	7.0	SqueezeNet	18	227×227	1.24
Inception-v3	48	299×299	23.9	VGG-16	16	224×224	128
MobileNet-v2	53	224×224	3.5	VGG-19	19	224×224	144

Table 2

Mixture proportioning of concrete sample, kg/m^{3}.

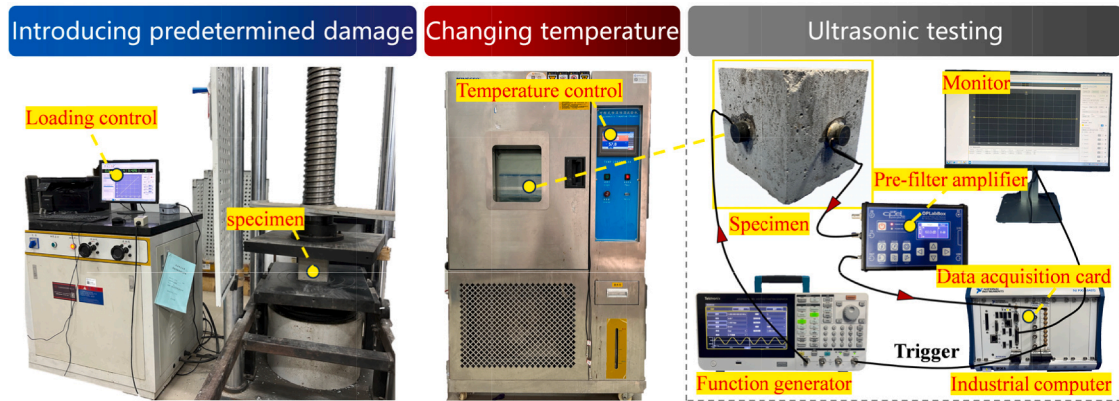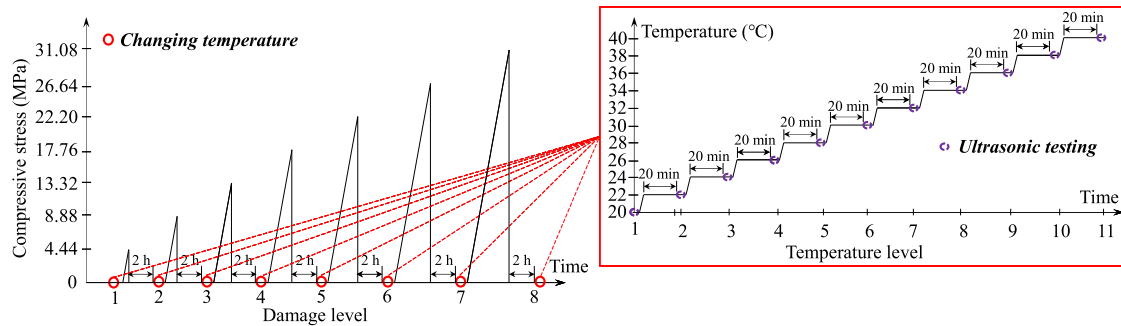| Composition	Cement	Water	Superplasticizer	Fine sand	Flyash	Aggregate
Quantity	345	178	12.1	840	71	900

Fig. 1. The overall experimental setups.

Fig. 2. The entire experimental procedure.

subjected to the compressive stress of 31.08 MPa. Furthermore, with an increase of the temperature, the waveforms at all damage levels generally show a decaying trend. The waveforms decay caused by a temperature change of 20 ℃ is significantly severer than that caused by damaged state with compressive stress of 31.08 MPa.

In this study, a swept frequency signal was used as the excitation signal. Therefore, in the time domain of the received signal, time corresponds to the scanning frequency. Since different frequency ranges respond differently to structural damage, using the peak-to-peak value of the entire signal cannot effectively describe the signal variation pattern. The time and frequency domains of a typical signal are shown in Fig. 4 (a) and Fig. 4 (b), respectively. Overall, there are three distinct maximum responses. Therefore, three time windows corresponding to the three frequency ranges are considered for calculating the peak-to-peak value of the signal. The three maximum responses appear within the ranges of [0——1.25] ms, [1.25——3.25] ms, and [3.25——5.5] ms, and their frequency spectrum are shown in Fig. 4 (c). Therefore, the peak-to-peak values are calculated within these three time ranges, respectively, as shown in Fig. 5. To compare the effects of damage and temperature changes on the signal peak-to-peak values, the signal measured in the undamaged state at 20 ℃ is used as the baseline. Fig. 5 (a) illustrates the variation in signal peak-to-peak values with increasing temperature in the undamaged state, while Fig. 5 (b) depicts the changes in signal peak-to-peak values with increasing damage at 20 ℃. As the temperature increases, the first wave peak consistently exhibits a downward trend, while the third wave peak initially increases before declining. Similar findings are presented in Fig. 5 (b). Nonetheless, the turning point for the decline in the third peak value attributed to damage occurs significantly later, manifesting only when the damaged state with compressive stress of 26.64 MPa. Overall, the peak-to-peak value variations caused by compressive damages are less significant than those induced by temperature changes.

To compare the effects of damage and temperature changes on the signal energy, the signal energy measured in the undamaged state at 20 ℃ is used as the baseline to plot the variations in signal energy collected from three specimens, as shown in Fig. 6. In Fig. 6, the load case represents the signal energy changes measured at 20 ℃ with increasing damage, while the temperature case represents
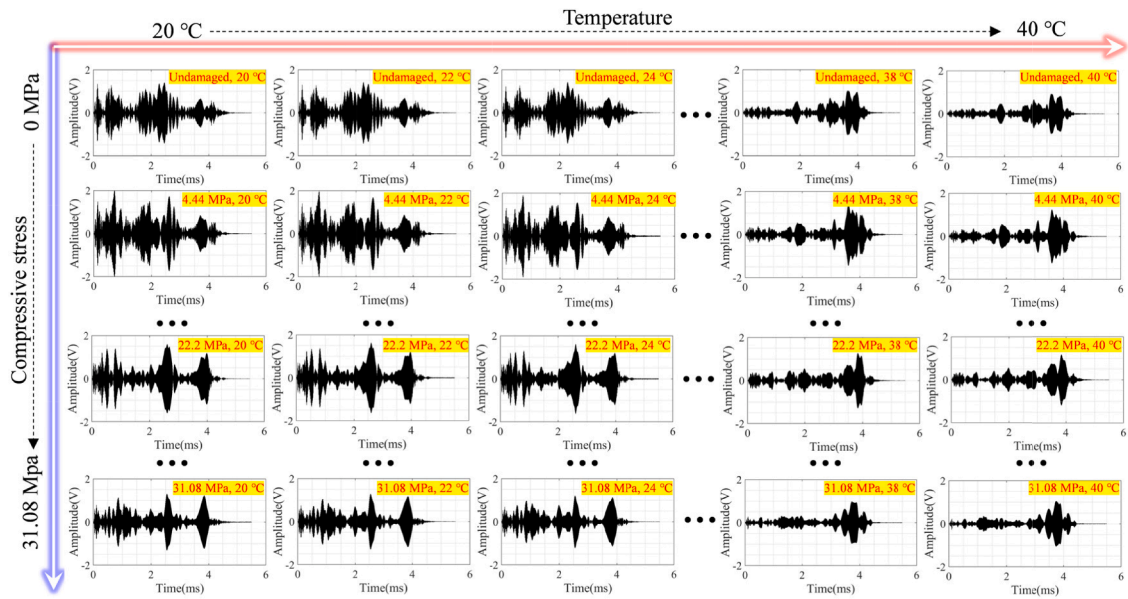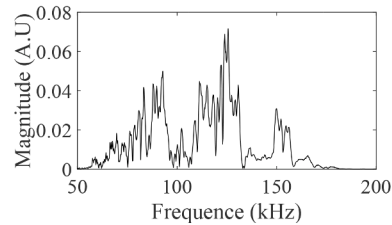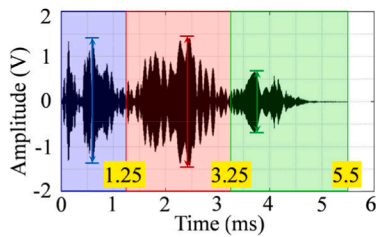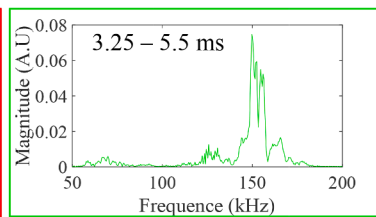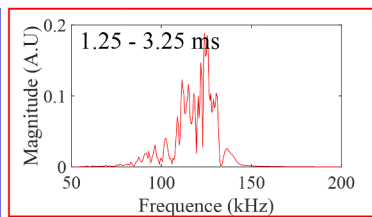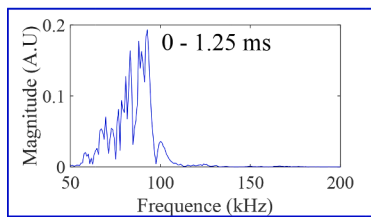
Fig. 3. Waveforms of specimen 1 under different temperatures and compressive damage states.
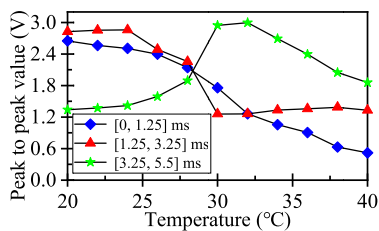

(a) The time domain of the entire signal   (b) The frequency domain of the entire signal
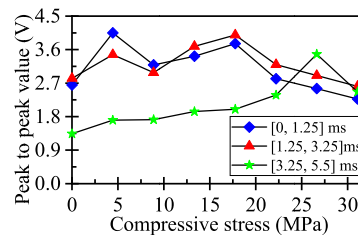

(c) The frequency domain of the segmented signals

Fig. 4. The time and frequency domains of a typical signal.

(a) Temperature changes   (b) Compressive damages

Fig. 5. Peak-to-peak values of specimen 1 subjected to temperature changes and compressive damages.
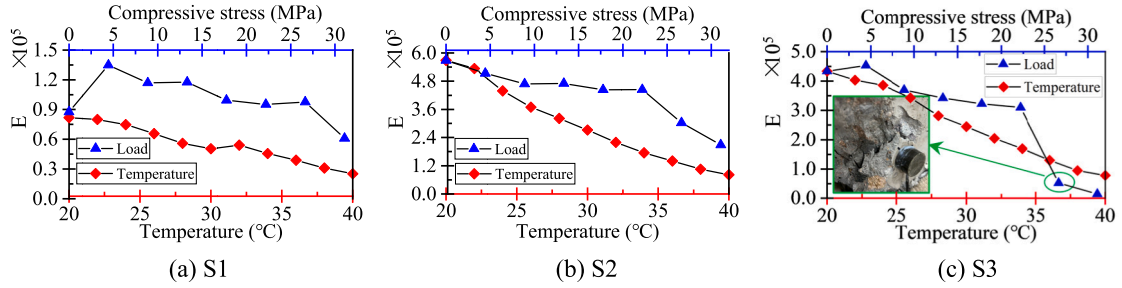
Fig. 6. Signal energy of specimen 1, 2, 3 subjected to temperature changes and compressive damages.

the signal energy changes measured in the undamaged state with increasing temperature. The signal energies of the three specimens with heating exhibit a uniform downward trend, whereas the energies under compressive load display a fluctuating downward trend. It is noted that only the energy attenuation experienced by specimen 3 under the damaged state with compressive stress of 26.64 MPa and 31.08 MPa exceeded that caused by a temperature increase of 20 ℃. The reason is attributed to that the concrete of specimen 3 around the receiving sensor was crushed under the compressive stress of 26.64 MPa, which led to partial detachment of the sensor.

4.2. Velocity change

Since the amplitude and energy parameters of ultrasonic signals may be influenced by the both performance of the sensor and the coupling layer under temperature changes [46]. This section aims to further discuss the signal characteristic changes caused by temperature changes and compressive damages by analyzing wave velocity changes. Fig. 7 presents the direct waves obtained from different temperatures and compressive damage states. Specifically, Fig. 7 (a) illustrates the direct waves under increasing temperature in the undamaged state, while Fig. 7 (b) depicts the direct waves with increasing damage at 20 ℃.

To quantify the wave velocity changes, the waveform stretching method is introduced [47]. This method maximizes the similarity between the perturbation signal and the baseline signal by stretching or compressing the perturbation signal. The stretching factor derived from this process represents the relative change in wave speed. This approach presents better accuracy and reliability compared to the direct selection of the first wave arrival time point on the waveform, as it eliminates the dependence on manual operations. The procedure is as following: initially, a transformation is applied to the perturbed signal X_1 using a time-domain scaling factor ε as Eq.(5), followed by performing a cross-correlation function with the initial waveform X_0 after the scaling transformation to determine the cross-correlation coefficient [48].

$$CC(\varepsilon) = \frac{\int_{t_1}^{t_2} X_1[t(1+\varepsilon)] \cdot X_0(t)dt}{\sqrt{\int_{t_1}^{t_2} X_1(t)^2 dt \cdot \int_{t_1}^{t_2} X_0(t)^2 dt}} \tag{5}$$

where t_1 and t_2 are the starting and ending of the selected time window, respectively. The ε_{max} corresponding to the maximum CC value is the relative speed change (dv/v) as Eq.(6):

$$\varepsilon_{max} = dv/v \tag{6}$$

Using the signal obtained at 20 ℃ in the undamaged state as the reference signal, the relative speed changes of signals from three specimens during heating and damage development were calculated using Eq. (5), as depicted in Fig. 8. In Fig. 8, the load case represents the relative velocity changes between the signals collected at 20 ℃ with increasing damage and the baseline signal, while
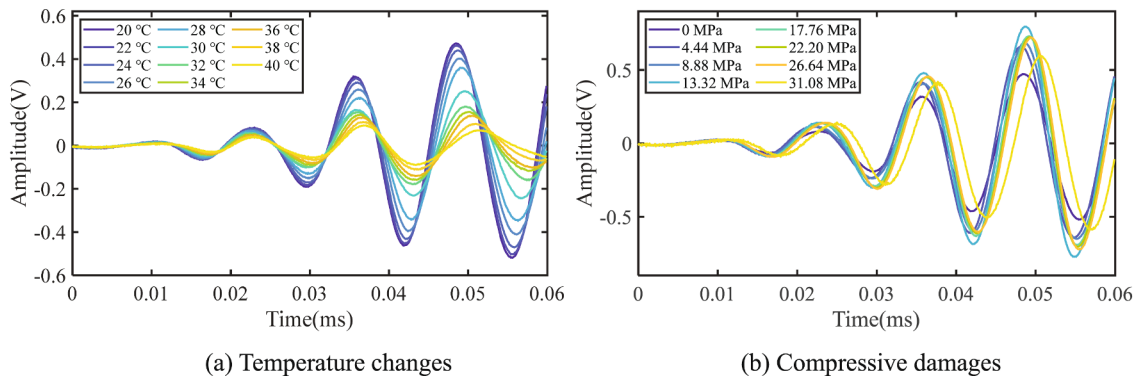

Fig. 7. The direct waves in specimen 1 under different temperatures and compressive damage states.

(a) S1   (b) S2   (c) S3
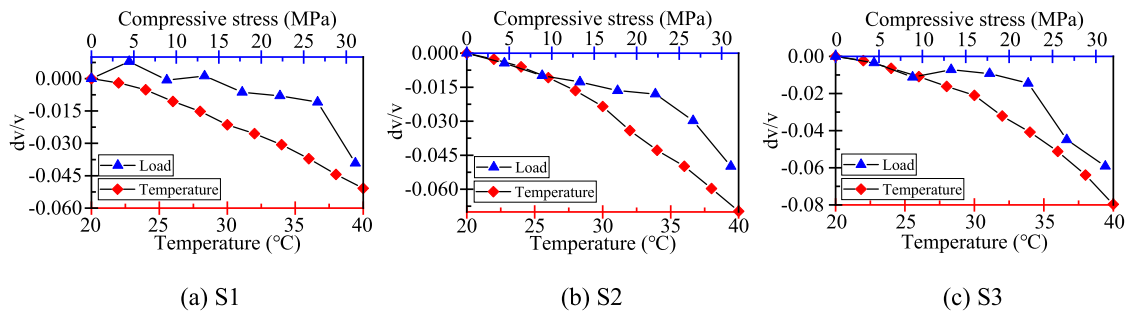
Fig. 8. The *dv/v* of specimen 1, 2, 3 subjected to both temperature changes and compressive damages.

the temperature case represents the relative velocity changes between the signals collected in the undamaged state with increasing temperature and the baseline signal. The *dv/v* values, resulting from the temperature rise in the three specimens, exhibit a consistent linear downward trend, indicating that the wave speed decreases as the temperature increases. However, the *dv/v* values attributable to compressive damage are not significant in the initial stages and exhibit a sudden drop in the final load stage before specimen failure. Overall, the relative speed changes caused by a temperature increase of 20 °C are more pronounced than those resulting from damaged state with the compressive stress of 31.08 MPa. The velocity changes cannot accurately characterize concrete compressive damage in environments with fluctuating temperatures.

4.3. Time-frequency spectrum

The analysis presented above demonstrates that both temperature increases and compressive damage can lead to reductions in the amplitude, energy, and speed of ultrasonic signals. Moreover, the changes in ultrasonic parameters induced by a temperature increase of 20 °C surpass those caused by compressive damage on the verge of failure under constant temperature conditions. Therefore, traditional ultrasonic characterization methods may fail in ultrasonic testing for concrete compressive damage under varying temperature environments.

All collected ultrasonic signals are converted into 2D time–frequency spectra using CWT. Due to space constraints, Fig. 9 partially presents the ultrasonic time–frequency spectra obtained from specimen 1 under different temperature conditions and various damage states, as detailed in the figure labels. Overall, despite the variations in temperature conditions and damage states, the general spectral characteristics remain consistent. The frequency distributions of the ultrasonic signals exhibit similarities across all time–frequency spectra. The frequency exhibits a linear variation with respect to time. The ultrasonic energy is primarily concentrated within the
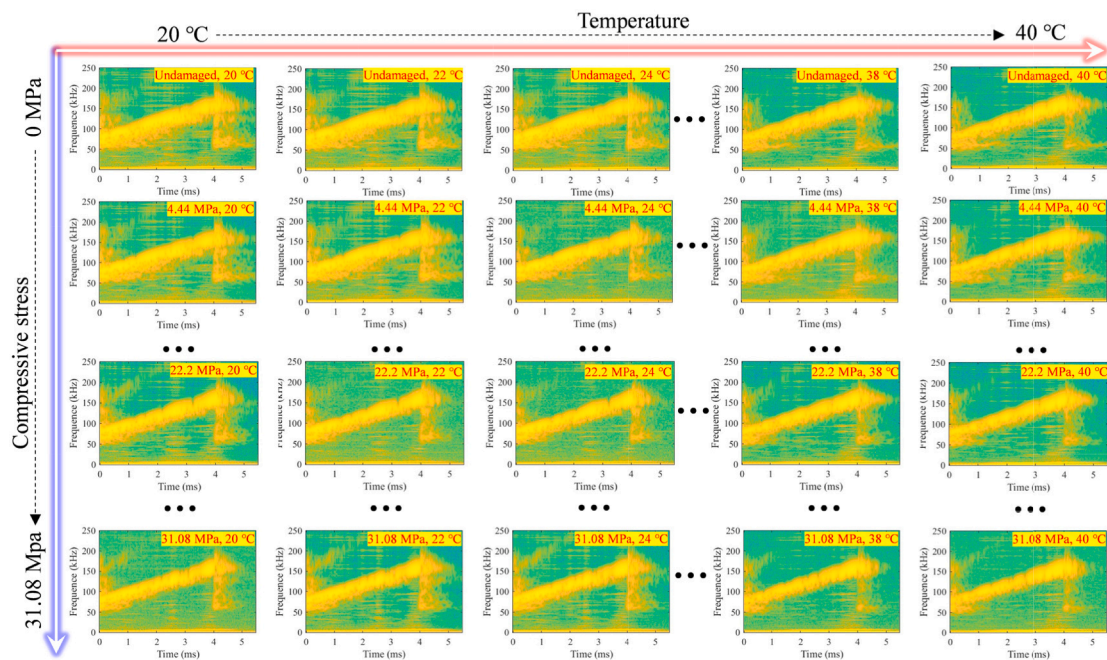

Fig. 9. Time-frequency spectra of specimen 1 under different temperatures and compressive damage states.

frequency range of 80 kHz to 160 kHz and the time range of 0 to 4 ms. These observations align with the excitation signal parameters employed in the experimental setup. The observed similarity in frequency distributions suggests that the fundamental propagation mechanisms of ultrasonic waves remain largely unaltered by the compressive damage and temperature changes. This highlights the robustness of the ultrasonic testing in detecting the concrete characteristics. However, closer examination of the time–frequency spectra may reveal subtle shifts in the frequency content. As the temperature increases, the frequency range of the concentrated energy in the time–frequency spectra gradually decreases. Under the same temperature conditions, the frequency distribution of the time-–frequency spectra exhibits relatively minor changes with the progression of damage. Furthermore, by examining the tail portion of the signals, specifically within the time range of 4 to 5.5 ms, it is observed that the time–frequency energy distribution exhibits greater consistency under different temperatures for a given damage state compared to that under varying damage states at the same temperature. These findings indicate that temperature and damage affect the propagation characteristics of ultrasonic waves in concrete differently. However, the changes in the time–frequency spectra observed by visual inspection are limited and cannot be quantitatively described. To achieve ultrasonic diagnosis of compressive damage in concrete under varying temperature conditions, DL techniques are employed to recognize the time–frequency spectra of the signals.

5. Proposed ultrasonic diagnosis method based on transfer learning enhanced deep convolutional neural networks

An automated ultrasonic diagnostic method for detecting concrete compressive damage amidst temperature variations is proposed in this study. One hybrid approach that integrates the ultrasonic sweep frequency testing, CWT, and TL enhanced DCNN techniques is proposed. In this hybrid approach, the ultrasonic time–frequency spectrum serves as the input, while TL, utilizing pre-trained models, is employed to boost the performance of models. The hybrid approach enables the models to automatically learn the damage signatures and accurately recognize the damage states directly from the ultrasonic signals acquired in environments with temperature fluctuations. The overall workflow of the proposed method is illustrated in Fig. 10.

The pre-trained DCNN models utilized in this study were originally trained on ImageNet dataset [39]. These models are being adapted to analyze the time–frequency spectrum of ultrasonic signals. Since these models were initially designed to classify 1,000 different categories, it is essential to modify them for application in ultrasound diagnosis. Firstly, the pixel dimensions of the ultrasonic time–frequency spectra are adjusted to match the input requirements of the pre-trained models, and the details are provided in Table 1. Subsequently, the convolutional layers are frozen for preserving their capability for deep and high-level feature extraction. However, the network parameters, including the weights and biases of the fully connected layers, are fine-tuned to align with the specific objectives of this research. Moreover, the output layer is reconfigured to classify eight types of damage states, reflecting the experimental setup of this study.

During the model training process, the cross-entropy function is selected as the loss, with its mathematical expression presented in Eq. (7):

$$\text{Loss} = -\frac{1}{n} \sum_{k=1}^{n} \left[y_k ln(t_k) + (1 - y_k) ln(1 - t_k) \right] \tag{7}$$

where n represents the number of damage states; t denotes the predicted result; y corresponds to the actual damage state. The gradient descent method is utilized to minimize the loss function value. These computations are coded and executed using the Deep Learning Toolbox in MATLAB version 2023a. The computational environment includes a desktop with an Intel Core™ i7-10700 CPU, featuring
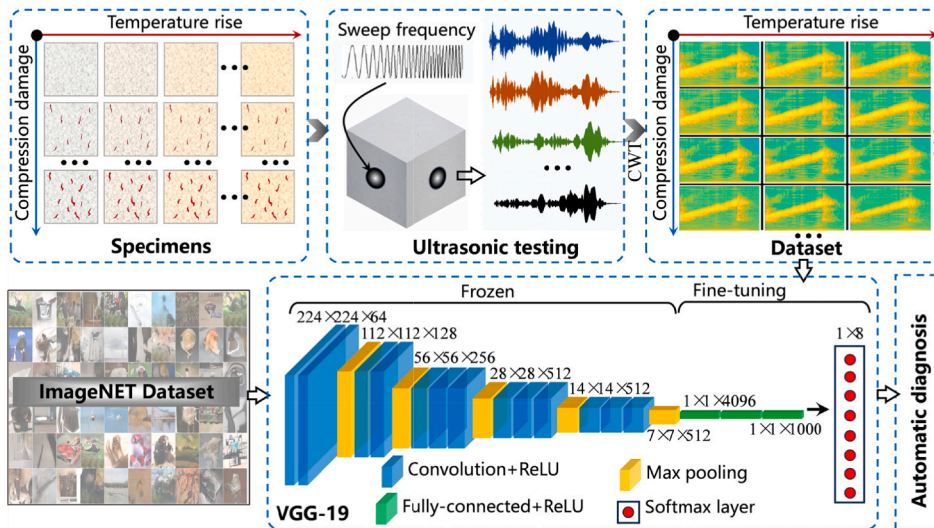

Fig. 10. The proposed ultrasonic diagnosis method based on TL enhanced DCNNs (taking VGG-19 as an example).

2.9 GHz, 8 cores, and an NVIDIA Quadro RTX 4000 GPU, which has 4608 cores, 576 Tensor cores, and 8 GB of memory.

6. Results and discussions

6.1. The performance of various DCNNs

In this section, 12 pre-trained DCNNs are used as backbone architectures for the ultrasonic diagnosis of concrete compressive damage amidst temperature variations. This study collected 264 ultrasonic signals from the three specimens, encompassing eight levels of damage with eleven different temperatures. All signals were transformed into time–frequency spectra using the CWT, which generate a dataset comprising 264 RGB images. Approximately 80 % of the time–frequency spectra for each level of compressive damage were allocated in the training set, with the remaining spectra forming the testing set. Consequently, the training and testing sets contain 26 and 7 images per damage level, respectively. It is noted that each damage label encompasses time–frequency images obtained at various temperatures. It would enhance the ability of DCNNs to discern damage features across a range of temperature conditions.

It is crucial to establish appropriate hyperparameters for DCNNs, as these parameters significantly influence the generalization capability of the networks. In this study, optimal values for various DCNN hyperparameters were determined by extensive tests. These parameters include the mini-batch size (*mbs*), maximum epochs (*mxe*), initial learning rate (*lr*), momentum (*mt*), learning rate drop period (*ldp*), weight decay factor (*l2r*), and learning rate drop factor (*ldf*), all of which are detailed in Table 3. Considering the number of training time–frequency images, the chosen mini-batch size and the maximum epochs are set to 32 and 100, respectively. Consequently, each DCNN model undergoes a total of 600 iterations during the training process.

Pretrained DCNNs serve as the source domain models, equipped with initial weights. Then, the DCNNs are adapted for ultrasonic diagnosis of concrete compressive damage by training a target domain model through a fine-tuning strategy based on transfer learning. Due to the space constraints, only the changes in accuracy and loss over iterations for the training and testing samples within the transfer learning model based on the AlexNet architecture are showcased, as depicted in Fig. 11. The accuracy for the training samples reached 100 % after 200 iterations and then gradually stabilized, so did the loss. The accuracy for the testing samples is slightly lower compared to the training samples, whereas the loss for the testing samples is marginally higher.

TL models with 12 different backbone structures were applied to the same dataset and validation set. The performance of these TL models is evaluated in the form of confusion matrix, including the number and proportion of true positive (TP), false positive (FP), true negative (TN) and false negative (FN), as illustrated in Fig. 12. Given the limited size of the dataset, a single incorrect prediction could result in approximately a 1.8 % variation of prediction accuracy. There is a significant disparity of prediction accuracy across different DCNN models, with values ranging from 57.1 % to 98.2 %. AlexNet demonstrated the highest predictive performance for ultrasonic diagnosis of concrete compressive damage amidst temperature variations, achieving an accuracy of 98.2 %. Other models achieving accuracy rates above 90 % include VGG-19 at 94.6 % and VGG-16 at 91.1 %.

To further evaluate the performance of different models, additional evaluation metrics were adopted, including Accuracy, Precision, Recall, F1 Score, Negative Predictive Value (NPV), and the Matthews Correlation Coefficient (MCC). Accuracy refers to the proportion of true positive and true negative cases among all the cases that the model predicted. A higher accuracy score demonstrates that the model excels at accurately identifying both positive and negative cases. Precision is a metric employed to evaluate the performance of a classification model, which measures the proportion of true positive cases among all the cases that the model predicted as positive. A higher precision score indicates that the model is better at avoiding false positives, which can be particularly important in applications where false positives are more costly than false negatives. Recall measure ability of models to correctly identify TP ranging from 0 to 1. A higher recall indicates better performance of the model in capturing TP. F1 Score is a metric that balances precision and recall, suitable for scenarios where FP and FN are equally important. It ranges from 0 to 1, with 1 indicating perfect precision and recall. NPV reflects the proportion of true negatives among those tested negative. MCC takes into account the TP, TN, FP and FN across all categories, offering a comprehensive assessment of performance. The range is from −1 to + 1, where + 1 indicates perfect prediction, 0 signifies an average random prediction, and −1 represents a completely discordant prediction. These evaluation metrics can be represented as following equations:

$$Accuracy = \frac{\sum_{i=1}^{N_{cl}}(TP_i + TN_i)}{\sum_{i=1}^{N_{cl}}(TP_i + FP_i + FN_i + TN_i)} \tag{8}$$

$$Precision = \frac{\sum_{i=1}^{N_{cl}}(TP_i)}{\sum_{i=1}^{N_{cl}}(TP_i + FP_i)} \tag{9}$$

Table 3
The optimal values of DCNN hyperparameters.

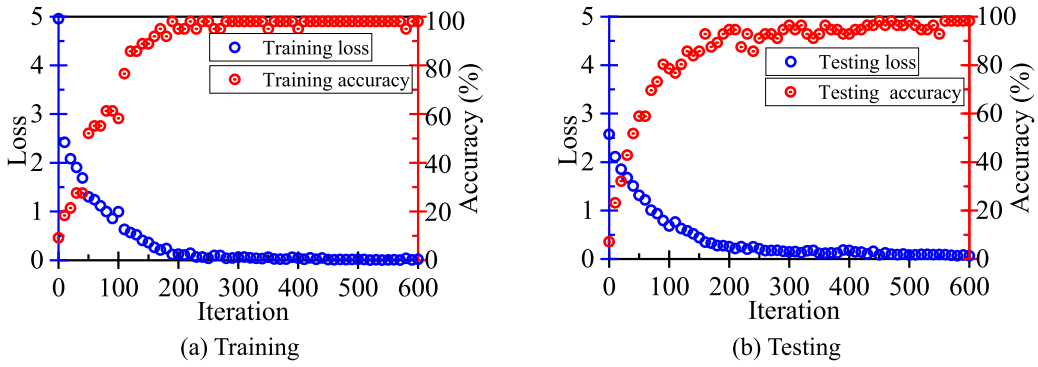| Parameter	*mbs*	*mxe*	*lr*	*mt*	*ldp*	*l2r*	*ldf*
Value	32	100	0.0001	0.9	5	0.0001	0.2

Fig. 11. Training and Testing loss and accuracy for a TL model based on the AlexNet backbone architecture.

$$Recall = \frac{\sum_{i=1}^{N_{cl}}(TP_i)}{\sum_{i=1}^{N_{cl}}(TP_i + FN_i)} \tag{10}$$

$$F_1\,Score = \frac{2 \bullet \frac{1}{N_{cl}}\sum_{i=1}^{N_{cl}}\frac{TP_i}{TP_i+FP_i} \bullet \frac{1}{N_{cl}}\sum_{i=1}^{N_{cl}}\frac{TP_i}{TP_i+FN_i}}{\frac{1}{N_{cl}}\sum_{i=1}^{N_{cl}}\frac{TP_i}{TP_i+FP_i} + \frac{1}{N_{cl}}\sum_{i=1}^{N_{cl}}\frac{TP_i}{TP_i+FN_i}} \tag{11}$$

$$NPV = \frac{\sum_{i=1}^{N_{cl}}(TN_i)}{\sum_{i=1}^{N_{cl}}(FN_i + TN_i)} \tag{12}$$

$$MCC = \frac{C \times S - \sum_k p_k \times t_k}{\sqrt{\left(S^2 - \sum_k p_k^2\right)\left(S^2 - \sum_k t_k^2\right)}} \tag{13}$$

where N_{cl} denotes the number of damage states, which is $N_{cl} = 8$ in this study, C represents the sum of all true positives across the matrix, S denotes the sum of all elements in the confusion matrix, p_k is the total predicted count for the kth column, t_k is the total actual count for the kth row.

Fig. 13 displays the radar charts for all evaluation metrics. Among these metrics, the TL models utilizing AlexNet as the backbone architecture consistently outperformed the others. The AlexNet emerges as the most effective pre-trained network for extracting time–frequency features of ultrasonic signals with the compressive damage under varying temperatures.

The t-Distributed Stochastic Neighbor Embedding (t-SNE) technique is utilized to illustrate the feature extraction process. As a machine learning algorithm, t-SNE specializes in dimensionality reduction and the visualization of high-dimensional data. The process initiates with the computation of the similarity similarity between data points in the high-dimensional space. This is typically achieved using the probabilities of a Gaussian distribution to represent the similarity between each pair of data points, with points of higher similarity being assigned higher probability values. Subsequently, t-SNE undertakes low-dimensional mapping by creating a corresponding point in a lower-dimensional space (generally 2D or 3D for visualization purposes) for each high-dimensional data point. The final step involves optimization, where t-SNE adjusts the positions of points in the low-dimensional space to minimize the Kullback-Leibler (KL) divergence between the similarity probability distributions in both high and low-dimensional spaces. A smaller KL divergence indicates a more accurate low-dimensional representation. The t-SNE analysis is performed on the input layer, the first FC layer, the second FC layer, and the last FC layer of the AlexNet model, as illustrated in Fig. 14. Initially, at the input layer, points representing different levels of damage are scattered and intermixed, demonstrating a lack of feature extraction by the TL model. However, as the TL model, which is well-trained, begins to learn damage recognition features from time-frequency images at various temperatures, these points start to converge into visually distinguishable clusters. This progression illustrates that the DCNN model is good at distinguishing between signal variations caused by changes in temperature and compressive damage.

6.2. The impact of training set temperature distribution for proposed method

To ensure that DL models maintain robust damage identification performance across various temperatures, it is crucial to include ultrasonic signals collected at a wide range of temperatures in the dataset. However, due to limitations in experimental conditions and labor costs, data collection is feasible only under specific temperature intervals. Consequently, this section investigates the impact of temperature distribution in the training set on the performance of the proposed ultrasonic diagnosis method for concrete compressive damage. To this end, four cases are designed: (a) continuously excluding higher temperatures, (b) continuously excluding lower temperatures, (c) continuously excluding moderate temperatures, and (d) intermittently excluding moderate temperatures from the training set. In each scenario, 1 to 5 groups of temperature data are systematically excluded, with the excluded data serving as the test
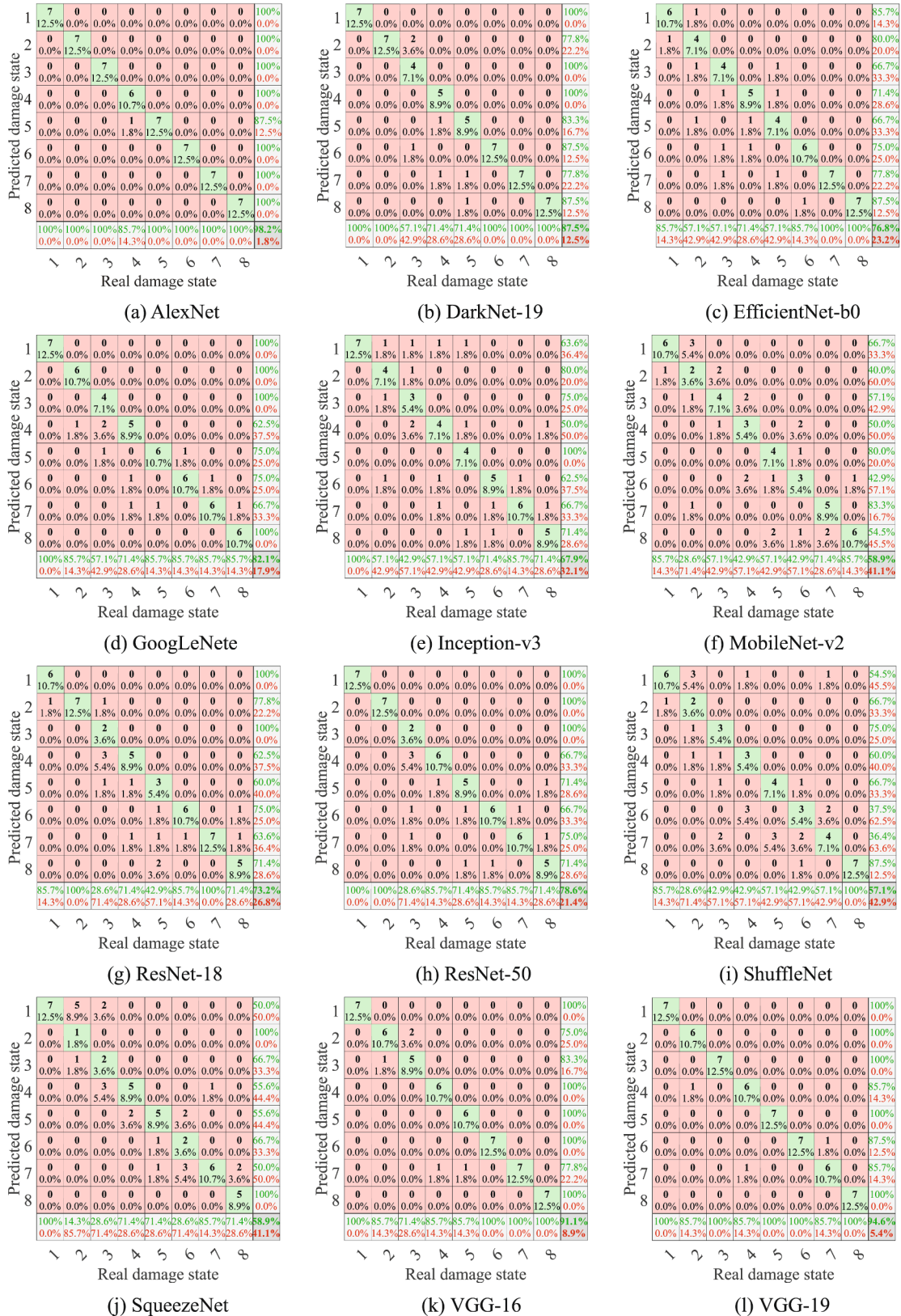
Fig. 12. Confusion matrices of different models for predicting testing dataset.
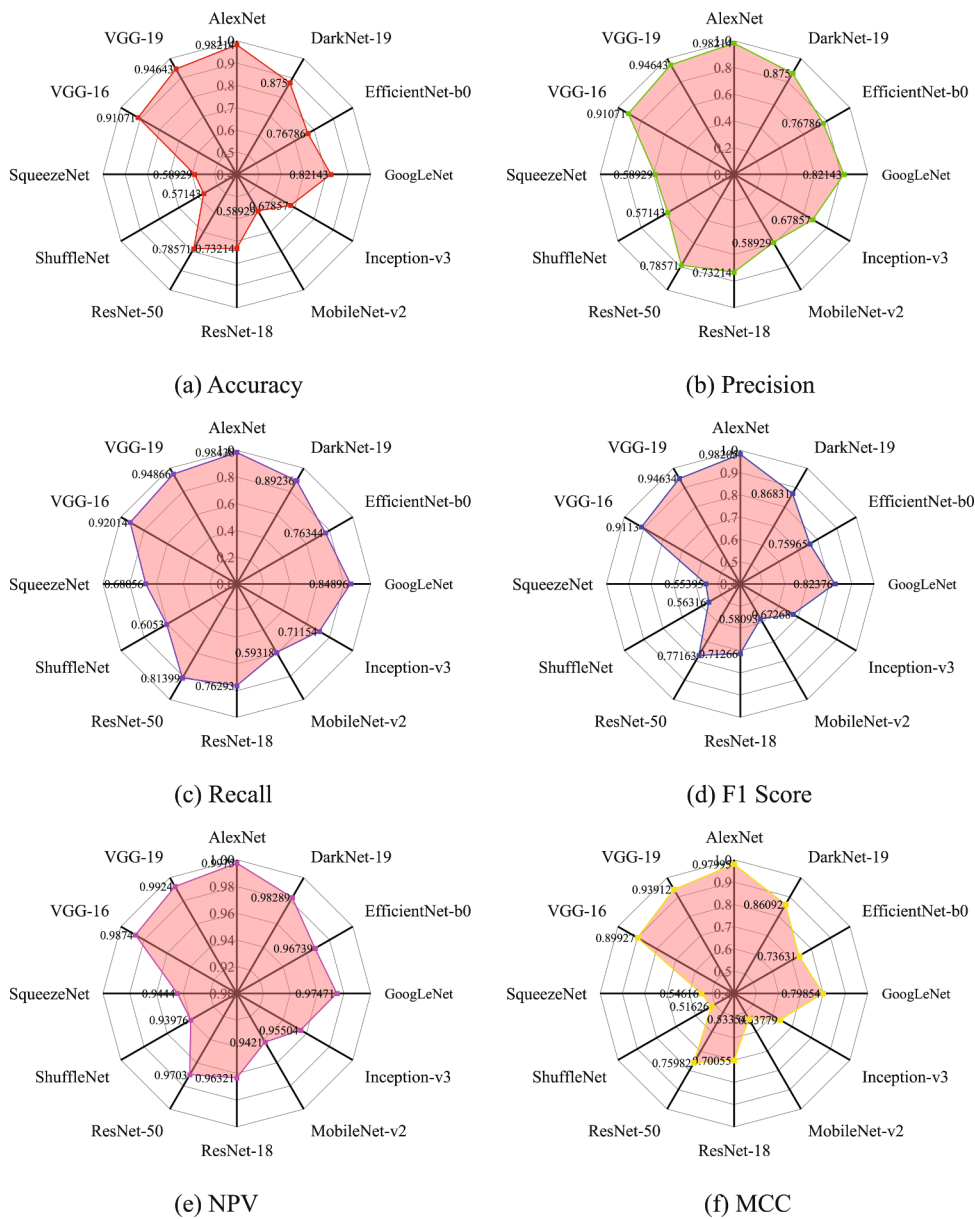
Fig. 13. Radar charts for different evaluation metrics.

set and the remaining data as the training set. The proportions of the training set accordingly are approximately 91 %, 82 %, 73 %, 64 %, and 55 %. It is noted that the test sets do not contain any temperature data from the training set to ensure complete separation and independence between them. The specific temperatures included in the training data are detailed in Table 4.

Ultrasonic diagnosis of concrete compressive damage is carried out using a TL model based on the AlexNet backbone architecture, which has been demonstrated to perform best in Section 6.1. Fig. 15 illustrates the identification accuracy across 20 scenarios in four distinct cases, revealing that Case 4 outperforms the others. In case 4, the accuracy remains relatively stable with the reduction in the proportion of training data, suggesting that the DL model is capable of accurately extracting damage-related information from temperature data with intervals of 4 ℃. To improve practicality, the temperature interval during sampling in the training set can be increased moderately. This DL-based method shows significant advantages over the traditional temperature compensation method, which relies on optimal baseline selection and recommends a reasonable temperature step between time-traces in a baseline dataset of 1 – 2 ℃ [25].

Upon analyzing Fig. 15 (a), (b), and (c), it is evident that DL models trained exclusively with lower temperatures demonstrate weaker generalization capabilities. As depicted in Fig. 15 (a), with a reduction in the proportion of training data, there is a rapid decline in accuracy. This issue is somewhat mitigated in Case 2, where the training set comprises only higher temperatures. However,
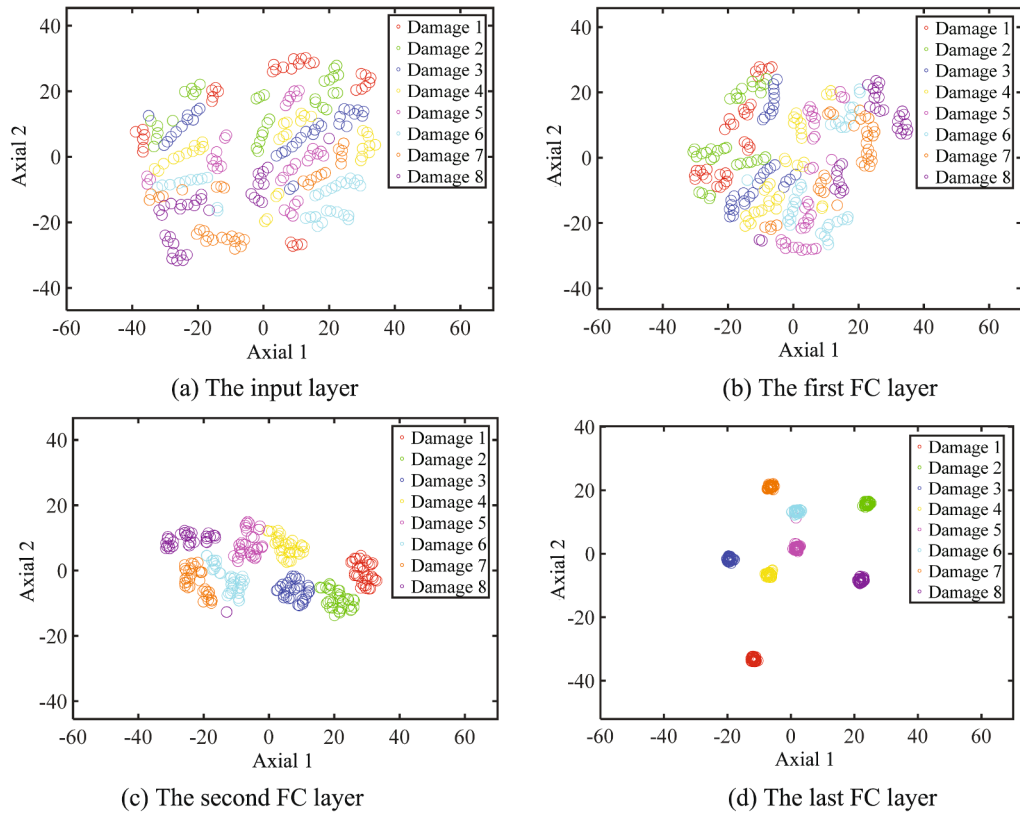
(a) The input layer

(b) The first FC layer

(c) The second FC layer

(d) The last FC layer

Fig. 14. T-SNE visualization results for TL model based on the AlexNet backbone architecture.

Table 4
Four cases for investigating the impact of training set temperature distribution.

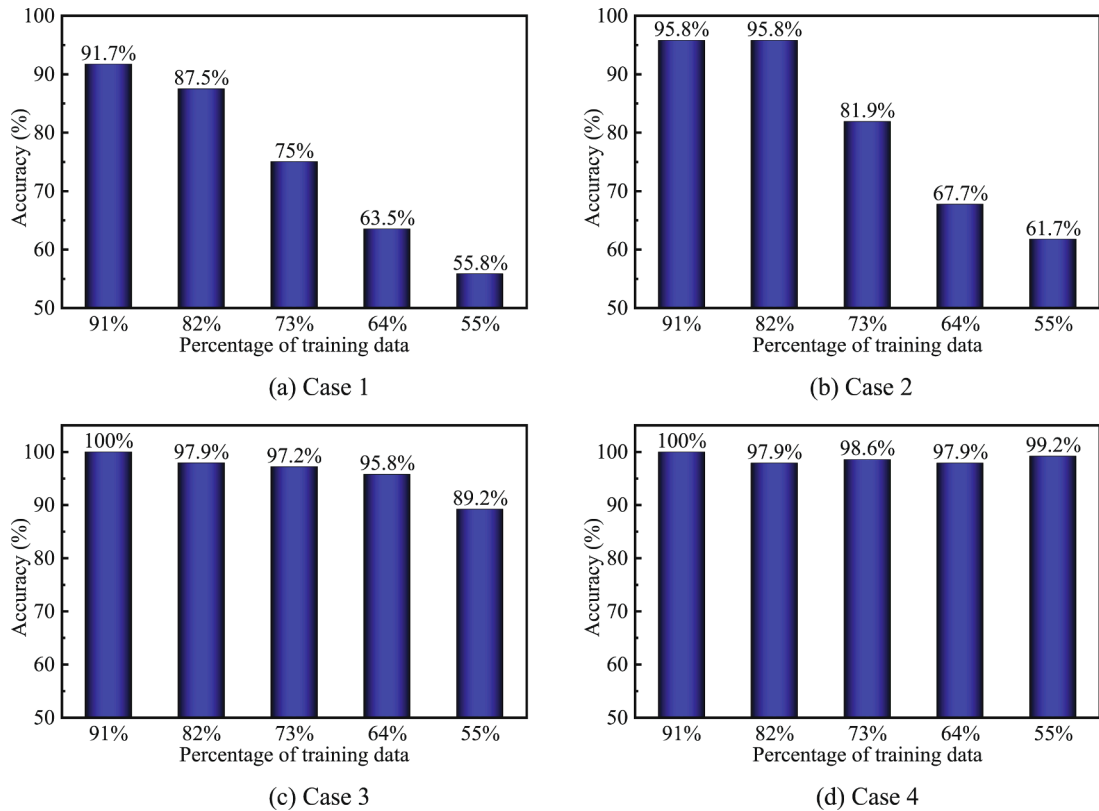| Case	Scenarios	Temperatures in training data	Percentage of training data
1	Excluding higher temperatures from the training set continuously	20 ℃, 22 ℃, 24 ℃, 26 ℃, 28 ℃, 30 ℃, 32 ℃, 34 ℃, 36 ℃, 38 ℃	91 %
		20 ℃, 22 ℃, 24 ℃, 26 ℃, 28 ℃, 30 ℃, 32 ℃, 34 ℃, 36 ℃	82 %
		20 ℃, 22 ℃, 24 ℃, 26 ℃, 28 ℃, 30 ℃, 32 ℃, 34 ℃	73 %
		20 ℃, 22 ℃, 24 ℃, 26 ℃, 28 ℃, 30 ℃, 32 ℃	64 %
		20 ℃, 22 ℃, 24 ℃, 26 ℃, 28 ℃, 30 ℃	55 %
2	Excluding lower temperatures from the training set continuously	22 ℃, 24 ℃, 26 ℃, 28 ℃, 30 ℃, 32 ℃, 34 ℃, 36 ℃, 38 ℃, 40 ℃	91 %
		24 ℃, 26 ℃, 28 ℃, 30 ℃, 32 ℃, 34 ℃, 36 ℃, 38 ℃, 40 ℃	82 %
		26 ℃, 28 ℃, 30 ℃, 32 ℃, 34 ℃, 36 ℃, 38 ℃, 40 ℃	73 %
		28 ℃, 30 ℃, 32 ℃, 34 ℃, 36 ℃, 38 ℃, 40 ℃	64 %
		30 ℃, 32 ℃, 34 ℃, 36 ℃, 38 ℃, 40 ℃	55 %
3	Excluding moderate temperatures from the training set continuously	20 ℃, 22 ℃, 24 ℃, 26 ℃, 28 ℃, 32 ℃, 34 ℃, 36 ℃, 38 ℃, 40 ℃	91 %
		20 ℃, 22 ℃, 24 ℃, 26 ℃, 28 ℃, 34 ℃, 36 ℃, 38 ℃, 40 ℃	82 %
		20 ℃, 22 ℃, 24 ℃, 26 ℃, 34 ℃, 36 ℃, 38 ℃, 40 ℃	73 %
		20 ℃, 22 ℃, 24 ℃, 26 ℃, 36 ℃, 38 ℃, 40 ℃	64 %
		20 ℃, 22 ℃, 24 ℃, 36 ℃, 38 ℃, 40 ℃	55 %
4	Excluding moderate temperatures from the training set intermittently	20 ℃, 22 ℃, 24 ℃, 26 ℃, 28 ℃, 32 ℃, 34 ℃, 36 ℃, 38 ℃, 40 ℃	91 %
		20 ℃, 22 ℃, 24 ℃, 26 ℃, 28 ℃, 32 ℃, 36 ℃, 38 ℃, 40 ℃	82 %
		20 ℃, 22 ℃, 24 ℃, 28 ℃, 32 ℃, 36 ℃, 38 ℃, 40 ℃	73 %
		20 ℃, 22 ℃, 24 ℃, 28 ℃, 32 ℃, 36 ℃, 40 ℃	64 %
		20 ℃, 24 ℃, 28 ℃, 32 ℃, 36 ℃, 40 ℃	55 %

Fig. 15. The accuracy of 20 scenarios across four cases for ultrasonic diagnosis.

the accuracy, with a decrease in the percentage of training data, remains unsatisfactory. In contrast, Case 3, where the test set includes data from the the higher and lower temperature ranges of the training set, exhibits higher accuracy. Specifically, Fig. 15 (c) illustrates that even with only 64 % of the training data, accuracy can achieve up to 95.8 %. This observation suggests that in practical applications, the temperature range of the training data should span the expected temperature range during the structural lifetime.

To further demonstrate the influence of training set temperature distribution on ultrasonic diagnosis, Fig. 16 displays the t-SNE visualization results for all cases with a training data percentage of 82 %. It is evident that the capability of AlexNet model to extract damage recognition features from time-frequency images significantly varies with the temperature distributions. From Case 1 to Case 4, the clusters formed by points representing different damage levels become more visibly distinct, indicating an improvement in the AlexNet model's ability to extract relevant signals. In conclusion, for the method proposed in this study, it is advisable to include both the highest and lowest temperatures encountered during the structural lifespan in the training set. Furthermore, it is beneficial for these temperatures to be as evenly distributed as possible.

7. Conclusions

To achieve automated ultrasonic diagnosis for concrete compressive damage amidst external temperature variations, this paper introduces a detection method that integrates ultrasonic sweep frequency testing, the CWT time–frequency spectrum, and TL technologies based on DCNNs. Ultrasonic testing experiments were conducted on concrete specimens subjected to compressive damages and temperature changes. Based on the results of these experiments and subsequent analysis, the following conclusions can be drawn:

(1) Temperature variations significantly interfere with the ultrasonic testing for detecting concrete compressive damage. The changes in ultrasonic parameters, such as peak-to-peak values, energy, and velocity induced by a temperature variation of 20 ℃, are more pronounced than those observed as the concrete specimens approach failure.
(2) By utilizing the time–frequency spectrum of ultrasonic signals as the input for models, TL techniques based on pre-trained DCNNs are capable of effectively extracting damage-sensitive features from ultrasonic signals under temperature variations, even in scenarios with limited data, for automated ultrasonic diagnosis. In this research, the AlexNet model achieved the optimal performance, reaching an accuracy of up to 98.2 %.
(3) After conducting tests across multiple training sets under various temperature distribution scenarios, it has been determined that to improve generalization capability of the model, the temperature range of the training data should encompass the entire expected temperature range during the lifespan of the concrete structure and should be as evenly distributed as possible.
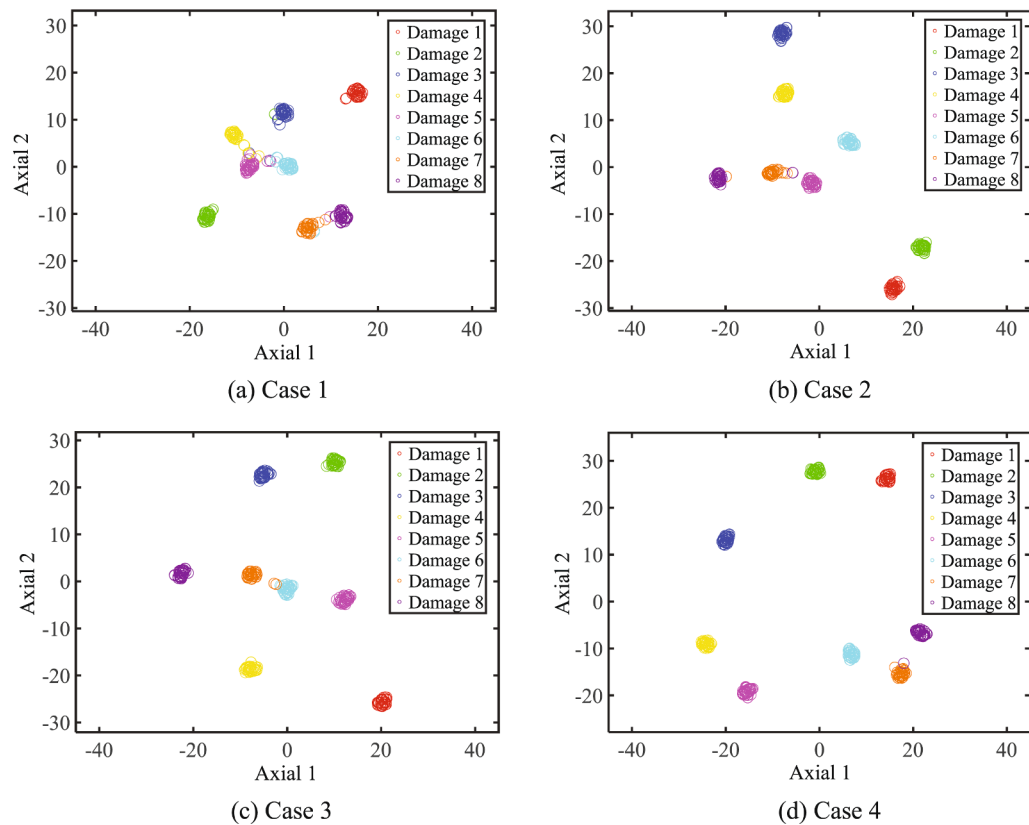
Fig. 16. T-SNE visualization results of the last FC layer for all cases with 82% percentage of training data.

This study predominantly employs linear ultrasonic features as inputs for deep learning models. As a class of ultrasonic methods renowned for their higher sensitivity, the combination of nonlinear ultrasonic and deep learning will be investigated to enhance the sensitivity in detecting minor damage in concrete. [49] Moreover, future research should prioritize the comprehensive evaluation of the generalization capability of the method across different specimens to enhance its reliability and practicality in real-world applications. This can be accomplished by expanding the experimental dataset to include a wide range of concrete specimens sourced from different batches, mixing proportions, and curing conditions. By incorporating this diversity in the study, valuable insights can be gained into the limitations of the method, and potential strategies for improvement, such as domain adaptation deep transfer learning methods [50,51], can be identified.

Funding

Declaration of competing interest

The authors declare that they have no known competing financial interests or personal relationships that could have appeared to influence the work reported in this paper.

Data availability

Data will be made available on request.

References

[1] X. Xu, B. Ran, N. Jiang, L. Xu, P. Huan, X. Zhang, Z. Li, A systematic review of ultrasonic techniques for defects detection in construction and building materials, Measurement 226 (2024) 114181, https://doi.org/10.1016/j.measurement.2024.114181.

[2] T. Planès, E. Larose, A review of ultrasonic Coda Wave Interferometry in concrete, Cem. Concr. Res. 53 (2013) 248–255, https://doi.org/10.1016/j. cemconres.2013.07.009.

[3] G. Karaiskos, A. Deraemaeker, D.G. Aggelis, D.V. Hemelrijck, Monitoring of concrete structures using the ultrasonic pulse velocity method, Smart Mater. Struct. 24 (2015) 113001, https://doi.org/10.1088/0964-1726/24/11/113001.

[4] J.S. Popovics, K.V.L. Subramaniam, Review of Ultrasonic Wave Reflection Applied to Early-Age Concrete and Cementitious Materials, J. Nondestr. Eval. 34 (2015) 267, https://doi.org/10.1007/s10921-014-0267-3.

[5] S. Basu, A. Thirumalaiselvi, S. Sasmal, T. Kundu, Nonlinear ultrasonics-based technique for monitoring damage progression in reinforced concrete structures, Ultrasonics 115 (2021) 106472, https://doi.org/10.1016/j.ultras.2021.106472.

[6] P. Antonaci, C.L.E. Bruno, A.S. Gliozzi, M. Scalerandi, Monitoring evolution of compressive damage in concrete with linear and nonlinear ultrasonic methods, Cem. Concr. Res. 40 (2010) 1106–1113, https://doi.org/10.1016/j.cemconres.2010.02.017.

[7] A. Castellano, A. Fraddosio, M.D. Piccioni, T. Kundu, Linear and Nonlinear Ultrasonic Techniques for Monitoring Stress-Induced Damages in Concrete, Journal of Nondestructive Evaluation, Diagnostics and Prognostics of Engineering Systems 4 (2021) 041001, https://doi.org/10.1115/1.4050354.

[8] R.M.L. Gondim, V.G. Haach, Monitoring of ultrasonic velocity in concrete specimens during compressive loading-unloading cycles, Constr. Build. Mater. 302 (2021) 124218, https://doi.org/10.1016/j.conbuildmat.2021.124218.

[9] A.A. Shah, Y. Ribakov, Ch. Zhang, Efficiency and sensitivity of linear and non-linear ultrasonics to identifying micro and macro-scale defects in concrete, Mater. Des. 50 (2013) 905–916, https://doi.org/10.1016/j.matdes.2013.03.079.

[10] G. Kim, G. Loreto, J.-Y. Kim, K.E. Kurtis, J.J. Wall, L.J. Jacobs, In situ nonlinear ultrasonic technique for monitoring microcracking in concrete subjected to creep and cyclic loading, Ultrasonics 88 (2018) 64–71, https://doi.org/10.1016/j.ultras.2018.03.006.

[11] A.A. Shah, Y. Ribakov, S. Hirose, Nondestructive evaluation of damaged concrete using nonlinear ultrasonics, Mater. Des. 30 (2009) 775–782, https://doi.org/ 10.1016/j.matdes.2008.05.069.

[12] A.A. Shah, S. Hirose, Nonlinear Ultrasonic Investigation of Concrete Damaged under Uniaxial Compression Step Loading, J. Mater. Civ. Eng. 22 (2010) 476–484, https://doi.org/10.1061/(ASCE)MT.1943-5533.0000050.

[13] C. Payan V. Garnier J. Moysan P.A. Johnson Applying nonlinear resonant ultrasound spectroscopy to improving thermal damage assessment in concrete J. Acoust. Soc. Am. 121 2007 EL125–EL130 10.1121/1.2710745.

[14] S.-J. Park, G.J. Kim, H.-G. Kwak, Characterization of stress-dependent ultrasonic nonlinearity variation in concrete under cyclic loading using nonlinear resonant ultrasonic method, Constr. Build. Mater. 145 (2017) 272–282, https://doi.org/10.1016/j.conbuildmat.2017.03.201.

[15] J. Chen, L. Zhang, Experimental study of effects of water–cement ratio and curing time on nonlinear resonance of concrete, Mater. Struct. 48 (2015) 423–433, https://doi.org/10.1617/s11527-013-0193-3.

[16] H. Hu, D. Li, L. Wang, R. Chen, X. Xu, An improved ultrasonic coda wave method for concrete behavior monitoring under various loading conditions, Ultrasonics 116 (2021) 106498, https://doi.org/10.1016/j.ultras.2021.106498.

[17] P. Fröjd, P. Ulriksen, Detecting damage events in concrete using diffuse ultrasound structural health monitoring during strong environmental variations, Struct. Health Monit. 17 (2018) 410–419, https://doi.org/10.1177/1475921717699878.

[18] S. Liu, B. Ma, Z. Ma, J. Sun, Q. Wang, K. Liu, Evaluation of the compressional damage evolution of ancient fired clay bricks using coda wave analysis, Journal of Building Engineering 49 (2022) 104071, https://doi.org/10.1016/j.jobe.2022.104071.

[19] F. Lanza Di Scalea, S. Salamone, Temperature effects in ultrasonic Lamb wave structural health monitoring systems, J. Acoust. Soc. Am. 124 (2008) 161–174, https://doi.org/10.1121/1.2932071.

[20] O. Putkis, R.P. Dalton, A.J. Croxford, The influence of temperature variations on ultrasonic guided waves in anisotropic CFRP plates, Ultrasonics 60 (2015) 109–116, https://doi.org/10.1016/j.ultras.2015.03.003.

[21] E. Niederleithinger, C. Wunderlich, Influence of small temperature variations on the ultrasonic velocity in concrete, in: Denver, Colorado, USA, 2013: pp. 390–397. https://doi.org/10.1063/1.4789074.

[22] J. Zhao, J. Wu, X. Chen, R. Zeng, Effect of Temperature on Ultrasonic Nonlinear Parameters of Carbonated Concrete, Materials 15 (2022) 8797, https://doi.org/ 10.3390/ma15248797.

[23] J.B. Harley, J.M.F. Moura, Scale transform signal processing for optimal ultrasonic temperature compensation, IEEE Trans. Ultrason., Ferroelect., Freq. Contr. 59 (2012) 6327494, https://doi.org/10.1109/TUFFC.2012.2448.

[24] Y. Lu, J.E. Michaels, A methodology for structural health monitoring with diffuse ultrasonic waves in the presence of temperature variations, Ultrasonics 43 (2005) 717–731, https://doi.org/10.1016/j.ultras.2005.05.001.

[25] A.J. Croxford, J. Moll, P.D. Wilcox, J.E. Michaels, Efficient temperature compensation strategies for guided wave structural health monitoring, Ultrasonics 50 (2010) 517–528, https://doi.org/10.1016/j.ultras.2009.11.002.

[26] Y. Zhang, O. Abraham, V. Tournat, A. Le Duff, B. Lascoup, A. Loukili, F. Grondin, O. Durand, Validation of a thermal bias control technique for Coda Wave Interferometry (CWI), Ultrasonics 53 (2013) 658–664, https://doi.org/10.1016/j.ultras.2012.08.003.

[27] Y. Zhang, O. Abraham, F. Grondin, A. Loukili, V. Tournat, A.L. Duff, B. Lascoup, O. Durand, Study of stress-induced velocity variation in concrete under direct tensile force and monitoring of the damage level by using thermally-compensated Coda Wave Interferometry, Ultrasonics 52 (2012) 1038–1045, https://doi. org/10.1016/j.ultras.2012.08.011.

[28] B. Herdovics, F. Cegla, Compensation of phase response changes in ultrasonic transducers caused by temperature variations, Struct. Health Monit. 18 (2019) 508–523, https://doi.org/10.1177/1475921718759272.

[29] H. Li, D. Ai, H. Zhu, H. Luo, Integrated electromechanical impedance technique with convolutional neural network for concrete structural damage quantification under varied temperatures, Mech. Syst. Sig. Process. 152 (2021) 107467, https://doi.org/10.1016/j.ymssp.2020.107467.

[30] S. Cantero-Chinchilla, P.D. Wilcox, A.J. Croxford, Deep learning in automated ultrasonic NDE – Developments, axioms and opportunities, NDT and E Int. 131 (2022) 102703, https://doi.org/10.1016/j.ndteint.2022.102703.

[31] J. Chen, L. Cao, G. Song, Detection of the pipeline elbow erosion by percussion and deep learning, Mech. Syst. Sig. Process. 200 (2023) 110546, https://doi.org/ 10.1016/j.ymssp.2023.110546.

[32] M.D.E. Candelaria, S.-H. Kee, Evaluation of thermal damages of concrete subjected to high temperatures using recurrent neural networks for ultrasonic pulse waves, Construction and Building Materials 407 (2023) 133416, https://doi.org/10.1016/j.conbuildmat.2023.133416.

[33] C. Zhang, Q. Yan, Y. Zhang, X. Liao, H. Zhong, Intelligent monitoring of concrete-rock interface debonding via ultrasonic measurement integrated with convolutional neural network, Constr. Build. Mater. 400 (2023) 131865, https://doi.org/10.1016/j.conbuildmat.2023.131865.

[34] S.T. Kuchipudi, D. Ghosh, Automated detection and segmentation of internal defects in reinforced concrete using deep learning on ultrasonic images, Constr. Build. Mater. 411 (2024) 134491, https://doi.org/10.1016/j.conbuildmat.2023.134491.

[35] S. Mariani, Q. Rendu, M. Urbani, C. Sbarufatti, Causal dilated convolutional neural networks for automatic inspection of ultrasonic signals in non-destructive evaluation and structural health monitoring, Mech. Syst. Sig. Process. 157 (2021) 107748, https://doi.org/10.1016/j.ymssp.2021.107748.

[36] S. Shao, S. McAleer, R. Yan, P. Baldi, Highly Accurate Machine Fault Diagnosis Using Deep Transfer Learning, IEEE Trans. Ind. Inf. 15 (2019) 2446–2455, https://doi.org/10.1109/TII.2018.2864759.

[37] H. Zhong, Y. Lv, R. Yuan, D. Yang, Bearing fault diagnosis using transfer learning and self-attention ensemble lightweight convolutional neural network, Neurocomputing 501 (2022) 765–777, https://doi.org/10.1016/j.neucom.2022.06.066.

[38] Y. Yu, A.N. Hoshyar, B. Samali, G. Zhang, M. Rashidi, M. Mohammadi, Corrosion and coating defect assessment of coal handling and preparation plants (CHPP) using an ensemble of deep convolutional neural networks and decision-level data fusion, Neural Comput. & Applic. 35 (2023) 18697–18718, https://doi.org/ 10.1007/s00521-023-08699-3.

[39] Y. Yu, B. Samali, M. Rashidi, M. Mohammadi, T.N. Nguyen, G. Zhang, Vision-based concrete crack detection using a hybrid framework considering noise effect, Journal of Building Engineering 61 (2022) 105246, https://doi.org/10.1016/j.jobe.2022.105246.

[40] X. Yin, Z. Huang, Y. Liu, Bridge damage identification under the moving vehicle loads based on the method of physics-guided deep neural networks, Mech. Syst. Sig. Process. 190 (2023) 110123, https://doi.org/10.1016/j.ymssp.2023.110123.

[41] S. Talaei, X. Zhu, J. Li, Y. Yu, T.H.T. Chan, Transfer learning based bridge damage detection: Leveraging time-frequency features, Structures 57 (2023) 105052, https://doi.org/10.1016/j.istruc.2023.105052.

[42] X. Liao, Q. Yan, H. Zhong, Y. Zhang, C. Zhang, Integrating PZT-enabled active sensing with deep learning techniques for automatic monitoring and assessment of early-age concrete strength, Measurement 211 (2023) 112657, https://doi.org/10.1016/j.measurement.2023.112657.

[43] Y. Yu, C. Zhang, X. Xie, A.M. Yousefi, G. Zhang, J. Li, B. Samali, Compressive strength evaluation of cement-based materials in sulphate environment using optimized deep learning technology, Developments in the Built Environment 16 (2023) 100298, https://doi.org/10.1016/j.dibe.2023.100298.

[44] Q. Xu, M. Solaimanian, Modeling temperature distribution and thermal property of asphalt concrete for laboratory testing applications, Constr. Build. Mater. 24 (2010) 487–497, https://doi.org/10.1016/j.conbuildmat.2009.10.013.

[45] X. Li, L. Chen, H. Chen, Q. Kong, HPSA: a high-performance smart aggregate for concrete structural health monitoring based on acoustic impedance matching method, Smart Mater. Struct. 32 (2023) 075007, https://doi.org/10.1088/1361-665X/acd60c.

[46] F. Lanza Di Scalea, H. Matt, I. Bartoli, The response of rectangular piezoelectric sensors to Rayleigh and Lamb ultrasonic waves, J. Acoust. Soc. Am. 121 (2007) 175–187, https://doi.org/10.1121/1.2400668.

[47] A. Deraemaeker, C. Dumoulin, Embedding ultrasonic transducers in concrete: A lifelong monitoring technology, Constr. Build. Mater. 194 (2019) 42–50, https://doi.org/10.1016/j.conbuildmat.2018.11.013.

[48] X. Sun, M. Zhang, W. Gao, C. Guo, Q. Kong, A novel method for steel bar all-stage pitting corrosion monitoring using the feature-level fusion of ultrasonic direct waves and coda waves, Struct. Health Monit. 22 (2023) 714–729, https://doi.org/10.1177/14759217221094466.

[49] J. Lee, S.E. Lee, S. Jin, H. Sohn, J.-W. Hong, An application of machine learning for material crack diagnosis using nonlinear ultrasonics, Mech. Syst. Sig. Process. 214 (2024) 111371, https://doi.org/10.1016/j.ymssp.2024.111371.

[50] Z. Liao, P. Qiao, Guided wave-based cross-scene interfacial debonding detection in reinforced concrete structures, Measurement 223 (2023) 113694, https://doi.org/10.1016/j.measurement.2023.113694.

[51] Y. Lin, Z. Nie, H. Ma, Dynamics-based cross-domain structural damage detection through deep transfer learning, Computer Aided Civil Eng 37 (2022) 24–54, https://doi.org/10.1111/mice.12692.